Graphene spintronics: Spin injection and proximity effects from first principles

P. Lazić,[1] G. M. Sipahi,[2,*] R. K. Kawakami,[3] and Igor Žutić[2,†]
[1]*Rudjer Bošković Institute, PO Box 180, Bijenička c. 54, 10 002 Zagreb, Croatia*
[2]*Department of Physics, University at Buffalo, State University of New York, Buffalo, New York 14260, USA*
[3]*Department of Physics, The Ohio State University, Columbus, Ohio 43210, USA*
(Received 17 February 2014; revised manuscript received 1 August 2014; published 22 August 2014)

Ferromagnet/graphene (F/Gr) junctions are important building blocks for graphene spintronics. While simple models of spin injection are very successful for macroscopic metallic junctions, they reveal many deficiencies in describing F/Gr junctions. First-principles methods are key to assess such Gr-based junctions, but the computational cost is often too high. We focus on Ni(111)/Gr junctions and include van der Waals interactions from first principles, crucial for their correct description. We formulate a computationally inexpensive model to examine the nonuniformity and bias dependence of spin injection and elucidate proximity effects using spin polarization maps. Our results could extend the applicability of simple spin injection models in F/Gr junctions.

DOI: 10.1103/PhysRevB.90.085429 PACS number(s): 85.75.−d, 81.05.ue, 72.25.Mk

I. INTRODUCTION

The discovery of graphene has quickly stimulated experiments to study its junctions with ferromagnets as a possible building block for spin-based devices [1–6]. Ferromagnet/graphene (F/Gr) junctions offer a number of desirable spin-dependent properties. In such structures graphene can provide effective spin filtering [7] or replace a tunnel barrier, having an advantage of low resistance and a small number of defects [8–10]. F/Gr junctions display magnetic proximity effects [11–16] and a robust spin injection, larger than in other materials [17–20]. Both phenomena induce a magnetic moment in graphene, which in the first case already occurs spontaneously in equilibrium, while the second case represents a nonequilibrium process [21,22].

A robust spin injection in graphene [17] has motivated a proposal to seamlessly integrated memory and logic [23]. For specific applications, such as network search engines, graphene-based magnetologic gates [24] could significantly outperform CMOS counterparts [23]. F/Gr junctions are also a building block of these magnetologic gates, which are closely related to the geometry for detecting spin injection and accumulation through a nonlocal magnetoresistance in lateral spin valves [21,25–27].

F/Gr junctions can sustain large current densities and are suitable spin injectors in a semiconductor [8,19], useful for spin lasers. Through the angular momentum transfer, the injection of spin-polarized carriers leads to a stimulated emission of circularly polarized light [28–31]. Spin lasers offer an improved performance, such as a threshold reduction for lasing, an enhanced bandwidth, and reduced parasitic frequency modulation, as compared to their conventional (spin-unpolarized) counterparts [32–40].

Despite the spin relaxation time being significantly shorter than initially suggested [26], with its high mobility graphene is still a desirable spin channel. The spin-encoded information can be maintained over length scales exceeding microns [18], enabling graphene to be used in on-chip spin interconnects [41]. Conventional metallic interconnects, relying on time-dependent voltage and current, are the key obstacle in the continued scaling of integrated circuits. In addition to their drawbacks, such as dynamical crosstalk between wires and RC bottlenecks, these interconnects are also increasingly the main source of energy consumption [42]. Graphene-based spin interconnects relying on modulating spin polarization of a *constant* charge current could overcome these limitations [41].

The exchange splitting and magnetic moment induced in graphene by the proximity effects of the deposited ferromagnet can be useful for spintronic devices [11,12]. To avoid short circuiting the Gr layer [14], it is suitable to consider ferromagnetic insulators, such as lattice-matched EuO [11,15]. Unlike conventional narrow-band gap semiconductors with large and tunable spin-orbit coupling [21], graphene [43] offers other means to electrically tune spin-dependent properties. By modifying the carrier density with a gate voltage to alter magnetic proximity effects, electrical control of the exchange bias and the transistor action is possible in F/Gr junctions [12,13,16,44].

These properties of F/Gr junctions suggest a wealth of opportunities, not limited to magnetically storing and sensing information, but also including processing and transferring information. To critically assess proposed advantages of graphene spintronics [18,23,26], it is important to obtain a detailed atomistic understanding of spin-dependent properties of F/Gr junctions.

Predictive first-principles studies could then provide tailoring material properties for desired applications. Their input could also guide developing graphene-specific phenomenological models for spin injection and magnetic proximity effects and exploring additional figures of merit, not limited to maximizing injected spin polarization, magnetoresistance, or induced exchange splitting. For example, a uniform spin injection is important for a reproducible operation of multiple magnetologic gates [23]. Can we predict, from first principles, which factors can influence such a uniformity in F/Gr junctions?

*On sabbatical leave from Instituto de Física de São Carlos, Universidade de São Paulo, Brazil.
†zigor@buffalo.edu

 ©2014 American Physical Society

A closer look at F/Gr junctions reveals several important challenges for a reliable first-principles analysis, even when it is applied to a simple case of a lattice-matched Ni(111)/Gr junction. At first glance, standard density functional theory (DFT), used to study spin injection and spin filtering in Fe/GaAs-based junctions [45,46] (also well lattice matched), appears a good approach. However, the analysis of F/Gr junctions presents additional difficulties in describing interfacial properties as the standard exchange correlation functionals [47] do not include nonlocal correlations resulting in van der Waals (vdW) interactions, crucial for bonding in Gr junctions. For example, such functionals predict no bonding for a bilayer Gr. We therefore use an approach [48,49] which has evolved from the initial vdW-DF proposal [50].

Even simple lattice-matched F/Gr interfaces are not fully translationally invariant. If we move along a F/Gr interface we expect spatial nonuniformities that will lead to a nonuniform spin injection. Experimental configurations would likely include a mosaic of different F/Gr arrangements with inequivalent spin-dependent properties. Unfortunately, using an actual F/Gr junction size for a computational cell to study this spatial dependency is computationally prohibitively expensive. The characteristic dimensions of F/Gr junctions in various other spintronic devices are a sizable fraction of microns and the F/Gr interface should be replaced by some effective approach using a computationally accessible size of a cell. Another complication is that typical first-principles studies are better suited to study equilibrium magnetic proximity effects than spin injection which is a nonequilibrium process, usually requiring a description of diffusive transport and a nontrivial bias dependence.

We overcome these underlying challenges by formulating a computationally inexpensive model which could also provide guidance for other building blocks in graphene spintronics, not limited to magnetologic gates. We present our results for the example of a Ni(111)/Gr junction, known both to provide effective example spin filtering [7] as well as an important test case to correctly identify suitable exchange functionals in vdW studies which would accurately describe bonding of graphene [49]. A similar approach is possible for well latticed-matched Co(0001)/Gr junctions [51,52].

The organization of our presentation is as follows: The motivation for our studies is further supported in Sec. II where we discuss a simple model of spin injection and some of its inadequacies to describe F/Gr junctions. In Sec. III we introduce our computational geometry and the specific vdW approach used. Then we describe different and inequivalent spin polarizations in Sec. IV and use them to infer the properties of spin injection and magnetic proximity effects. We end this paper by providing conclusions and open questions for future work.

II. A SIMPLE MODEL OF SPIN INJECTION

One of the key elements in spintronics is generating spin imbalance or spin accumulation, typically realized by electrical spin injection from a ferromagnet into a nonmagnetic (N) region [21]. To summarize a simple model of spin injection [21,53–56] and understand its potential limitations

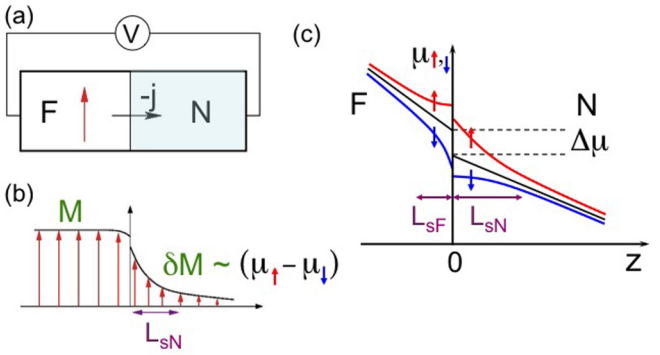

FIG. 1. (Color online) Electrical spin injection from a ferromagnet (F) into a nonmagnetic region (N). Electrons flow from F to N: (a) schematic device geometry and (b) the magnetization M can deviate from its equilibrium value M_0. Nonequilibrium magnetization δM (spin accumulation) is injected into N region at a characteristic length scale—the spin diffusion length L_{sN} for a nonmagnetic region; (c) spatial variation of the chemical potentials. At the F/N interface $z = 0$ the spin-resolved $\mu_{\uparrow,\downarrow}$ and the average chemical potentials are discontinuous. The spin diffusion length L_{sF} and L_{sN} can differ greatly [57].

in describing F/Gr junctions, it is helpful to define the spin polarization [21]

$$P_X = X_s/X \tag{1}$$

as the ratio of the difference $X_s = X_\lambda - X_{-\lambda}$ and the sum $X = X_\lambda + X_{-\lambda}$ of the spin-resolved λ components for a particular quantity X. A charge current j across the F/N junction, depicted in Fig. 1, results in the spin injection and spin accumulation in the N region.

The key result for spin injection can be expressed using spin polarizations and resistances [21,53,58]

$$P_j = [r_c P_\Sigma + r_F P_{\sigma F}]/r_{FN}, \tag{2}$$

where $r_{FN} = r_F + r_c + r_N$ is the effective equilibrium resistance of the F/N junction. The additive contributions for the F, contact, and N regions are given by $r_F = L_{sF}\sigma_F/(4\sigma_{\uparrow F}\sigma_{\downarrow F})$, $r_c = \Sigma/4\Sigma_\uparrow\Sigma_\downarrow$, and $r_N = L_{sN}/\sigma_N$, where $\sigma_{F,N}$ and Σ are N,F and contact conductivities, while $L_{sN,F}$ are the spin diffusion lengths (Fig. 1).

As shown by Petukhov [59], Eq. (2) follows from a simple equivalent circuit in Fig. 2, $P_j = -P_{\tilde{R}} \equiv -(\tilde{R}_\uparrow - \tilde{R}_\downarrow)/(\tilde{R}_\uparrow + \tilde{R}_\downarrow)$. The simplicity of Eq. (2) or Fig. 2 and the

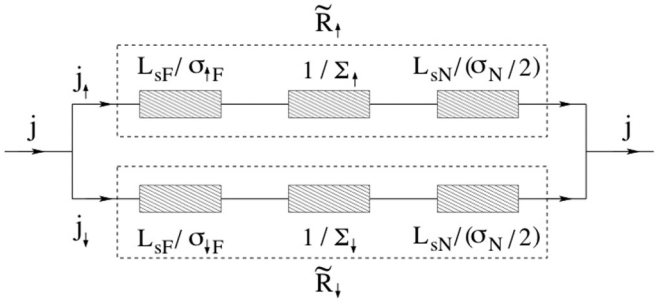

FIG. 2. Equivalent resistor scheme for spin injection across F/N junction in a linear regime.

analytical description of spin injection is very appealing. For transparent contacts $r_c = 0$, a resistance mismatch $r_F \ll r_N$ implies an inefficient spin injection: $P_j \approx r_F/r_N \ll 1$ [60]. A spin-selective resistive contact $r_c \gg r_F, r_N$ gives an effective spin injection $P_j \approx P_\Sigma$, dominated by the effect r_c and not by r_F/r_N [53,61].

This underlying simplicity represents well the linear regime in metallic junctions, expected also from the linear nature of the resistor scheme. Deviations from local charge neutrality, band bending, nonlinear current-voltage characteristics, an explicit bias dependence of spin injection, and the presence of both electrons and holes are neglected in this approach [62]. Relaxing these assumptions may lead to a qualitatively different behavior and the prediction of a spin accumulation spatially *enhanced* away from the point of spin injection [63], suggested to be also relevant for graphene junctions [26].

In F/Gr junctions various deviations from a simple resistor model of spin injection can occur. I-V nonlinearities are also present and the efficiency of spin injection is bias dependent, with an experimentally confirmed influence of the carrier drift [64]. However, disentangling this dependence is a challenging task. One also expects that an applied bias will modify the spin relaxation time [65,66] and alter the decay length of spin accumulation L_{sN}.

Other limitations of the resistor model for spin injection arise from its macroscopic character. A change from a single layer to bilayer graphene can have important implications for spin injection in F/Gr junctions. In addition to the gap opening in bilayer graphene, there could be a pronounced effect of spin filtering [7], altering the efficiency of spin injection. The choice of substrate, as we argue in Sec. IV, affects the uniformity of spin injection.

With effectively the one-dimensional character of this model, the spatial nonuniformity of spin injection along the F/N interface [recall Fig. 1(a)] is neglected. However, even a multidimensional generalization of a simple macroscopic model may overlook different intrinsic sources of spatial nonuniformities which can be explored from an atomically resolved interfacial structure. A strong correlation between such interfacial information obtained from first principles and the efficiency of spin injection has been confirmed experimentally in Fe/GaAs junctions [45]. We expect a similar situation in F/Gr junctions. A local change in the interfacial structure results in magnetically inequivalent environments for the C atoms and spatially changing spin-dependent properties.

This model also neglects the magnetic proximity effects, present at zero bias. The equilibrium properties of the N region are spin independent. Applied to graphene, at equilibrium there would be no induced magnetic moment, nor exchange splitting. First-principles studies can overcome such limitations and predict atomically resolved magnetic moments and exchange splitting.

While this simple model could be generalized to F1/N/F2 junctions [21,67], we will focus on F/Gr junctions, such as Ni(111)/Gr. Our findings, such as the energy dependence of the spin-resolved density of states calculated from first principles, may recover a part of the expected bias dependence of spin injection.

III. COMPUTATIONAL GEOMETRY

While a fully realistic description of a nonequilibrium process such as spin injection in graphene-based micron-sized devices is computationally inaccessible from first principles, important information can already be extracted from much smaller computational cells. Here we describe a computationally inexpensive model of F/Gr junctions that could provide atomically resolved information and explore various trends that may not be accessible from a simple model of spin injection or a phenomenological description of magnetic proximity effects.

In choosing the computational geometry, we focus on several simplifying assumptions which will help us to examine the nonuniformity of spin injection across F/Gr junctions, relevant for not only magnetologic gates, but also for using graphene in spin lasers and spin interconnects. However, elucidating spin-dependent properties of F/Gr junctions from first principles is important for magnetic proximity effects and has broader implications for graphene spintronics.

We choose a flat Ni(111)/Gr interface with no tunnel barrier [68]. Despite the good lattice match between Ni(111) and Gr (1% difference), moiré patterns, a signature of different interfacial configurations, have been observed not only in polycrystalline [69], but also in single-crystalline Ni [70]. We therefore calculate the properties for several interfacial configurations that may be present along the F/Gr interface. Our results include three high symmetry positions of the carbon atoms in the unit cell: top-fcc, top-hcp, and hcp- fcc, shown in addition with the reference Ni(111) surface in Fig. 3. Green lines mark the computational cell for the Ni slab and graphene (five- and two-atom cell, respectively).

If these different configurations are energetically similar, but lead to significantly different interfacial spin polarizations, we then expect a nonuniform spin injection. This connection also follows from Sec. II, as spin injection is related to the interfacial spin polarization. Another source of inhomogeneity is the formation of charge puddles in graphene [71] which

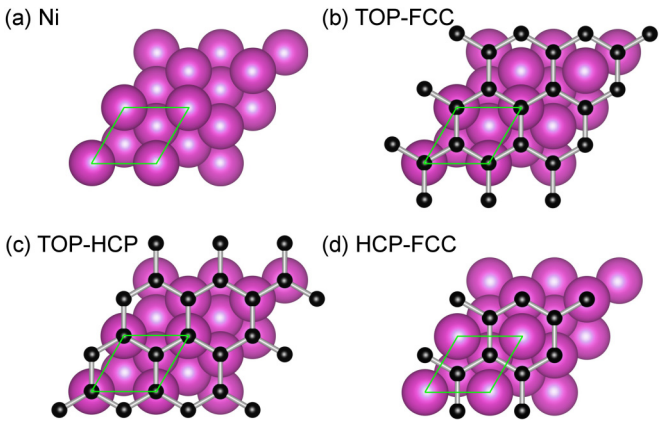

FIG. 3. (Color online) (a) Ni(111) bare surface and (b)–(d) with graphene adsorbed—top view. Carbon atoms are black and nickel atoms are violet. The unit cell is denoted by a green line. Studied interfacial configurations are labeled by the corresponding high symmetry position of the carbon atom in the unit cell: (b) top-fcc, (c) top-hcp, and (d) hcp-fcc.

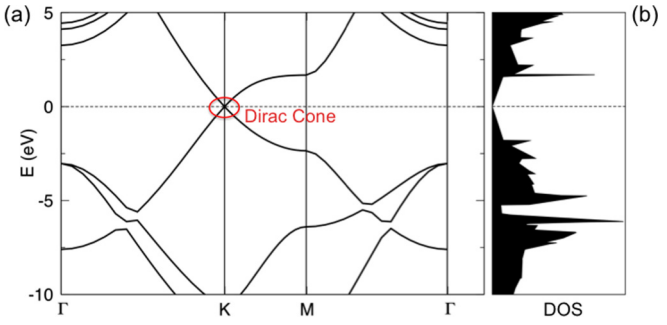

FIG. 4. (Color online) (a) Band structure of graphene with a marked Dirac cone at the K point. (b) The density of states (DOS) has pronounced peaks, expected from the flat-band regions in (b). The results have been calculated from first principles using the same set of parameters as described in the text.

leads to a substrate-dependent spatial variation of the chemical potential that we can model by a rigid shift in the electronic structure and an effective spin polarization.

To compute the properties of the considered Ni(111)/Gr configurations, we have used the Kohn-Sham DFT [72] with PAW pseudopotentials [73] in VASP 5.1 [74,75]. The correlation and the exchange part of the functional was vdW-DF and optB88, for the best agreement with the RPA results [49]. The inclusion of vdW interactions becomes particularly important for multilayer graphene with the interlayer binding having a predominantly vdW character. The plane wave cutoff was 500 eV, with a k-point density of $9\times9\times1$ [76].

A simple test of our approach and a reference for the influence of the added F region is provided by showing results for freestanding graphene in Fig. 4. Electronic structure calculations illustrate the implications of a two-atom unit cell which leads to two band crossings per Brillouin zone at the K and K' points. The band structure of graphene is shown in Fig. 4 along the directions given by the symmetry points of Γ, K, and M of the hexagonal Brillouin zone. The energy in Fig. 4, and in the subsequent results for the electronic structure, is measured with respect to the Fermi level. The conduction and valence band only touch in the charge neutrality points (only the K point is shown), forming Dirac cones with linear dispersion. Flat-band regions in Fig. 4(a) give rise to the peaks in the density of states shown in Fig. 4(b), which also reflects the presence of the Dirac cone at the Fermi level.

We next turn to the calculation of the electronic structure for Ni/Gr junctions [77]. A computational cell includes two C atoms per Gr layer (C1, C2) and the Ni(111) slab was simulated by five layers (one atom Ni per layer: Ni1, . . . , Ni5). Unless explicitly specified, our Ni/Gr slab structure was separated by 15 Å of vacuum in the z direction, from its periodic image. The bottom Ni layer (atom Ni5) was fixed, while other layers, including graphene, were allowed to relax, until the forces on atoms were below 1 meV/Å. After the full relaxation, the geometry we obtain has top-fcc as lowest-energy configuration, shown in Fig. 3(b). This is in agreement with both the experiments and the RPA results from Ref. [49], giving a binding distance ≈2.1 Å between the C1 and Ni1 interfacial atoms, where C1 is in the lower left part of the marked unit cell in Fig. 3(b), above Ni1 [78].

The spin-resolved band structure and DOS are shown in Fig. 5, where we take the graphene lattice constant (2.46 Å) to fit to the one of Ni (2.48 Å). This good lattice match is also reflected in nearly identical dashed reference curves for the band structure of freestanding Gr calculated at its own and as adjusted to the Ni lattice constant, shown for spin-up and spin-down in Figs. 5(a) and 5(c), respectively. We see that the presence of Ni introduces significant changes in the band structure, as well as in the DOS from Fig. 5(b), compared to pristine Gr in Fig. 4(b).

To understand the hybridization in a Ni/Gr junction it is helpful to invoke the results for freestanding Gr. The band structure in Fig. 5 acquires an explicit spin dependence and many states originating from Ni are visible near the Fermi level and a few eV below. Thicker lines denote states localized mainly on C atoms. The Dirac cone from Fig. 4 is destroyed and there is an opening of a spin-dependent energy gap. In Sec. IV we will revisit these features as a manifestation of the proximity effects.

Further information about the Ni/Gr electronic structure is provided by the atom-projected DOS in Fig. 6. For a given spin projection there is a slight DOS difference among the five Ni atoms, the DOS spin asymmetry is position dependent. A larger Ni DOS contribution for $E < 0$ than for $E > 0$ near the Fermi level is consistent with a stronger destruction of the K point Dirac cone at $E < 0$ in Fig. 5. This is pronounced for the

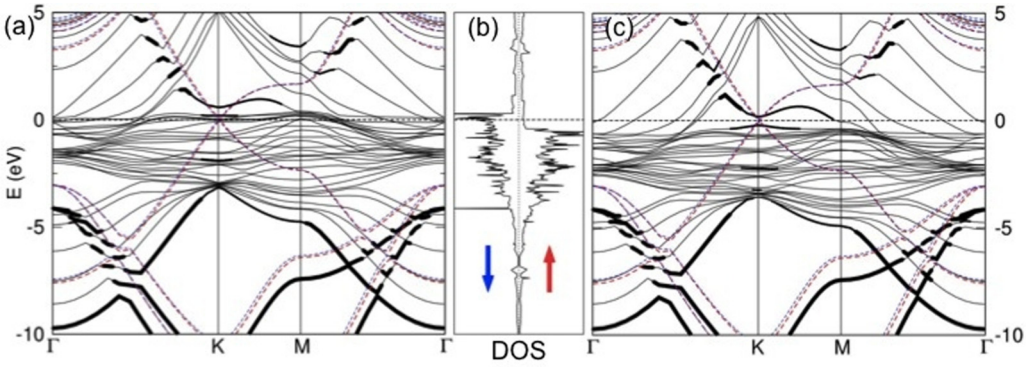

FIG. 5. (Color online) Top-fcc Ni/Gr [see Fig. 3(b)]. (a) and (c) Band structure for spin up/down. Thick lines: States localized mainly on C atoms. Red and blue dashed lines: Band structure of freestanding Gr at natural and Ni-adjusted lattice constants, respectively. (b) Density of states (DOS) for the two spins. In all the graphs the energy is measured with respect to the Fermi energy.

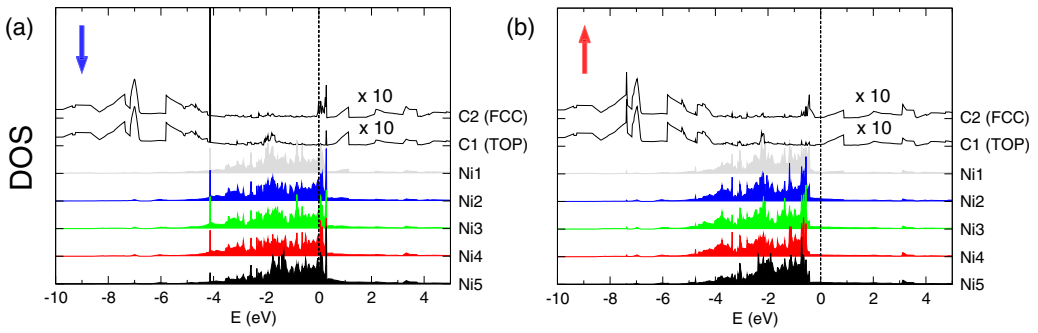

FIG. 6. (Color online) Atom-projected density of states (DOS) for top-fcc Ni/Gr. The data for each atom are shifted along the y axis for clarity. (a) The minority and (b) majority spin channels. The values for C atoms are scaled by a factor of 10.

spin-down channel with a nearly flat band around the K point at the Fermi level, strongly localized on C atoms (thick black line).

The DOS for C1 and C2 atoms, corresponding to top and fcc sites [see Fig. 3(a)], reveals differences with (i) respect to freestanding Gr and (ii) each other. Near the Fermi level a stronger influence of Ni is seen in the C1 DOS, while some of the features from freestanding Gr [Fig. 4(b)] are partially preserved in the C2 DOS. With a small Ni spin-up DOS for $E \gtrsim 0$, the same can also be expected for C2 which, compared to C1, is spatially further removed from the closest Ni atom. The smallest change in the Dirac cone from Fig. 4(b) is seen for the spin-up C2 DOS and $E > 0$ in Fig. 6(b). However, even there the DOS is visibly altered. While DOS $\propto E$ up to $E \sim 2$ eV in Fig. 4(b), such a linear Dirac-cone dependence already ends at $\sim$1 eV for C2 in Fig. 6(b), expected from the Ni-hybridization induced flattening of the C-localized band along the K-M direction in Fig. 5(c). Through interaction with Ni, other deviations in the C1 and C2 DOS from freestanding graphene, such as an overall shift in features at $E < 0$, are visible.

Complementary information about the hybridization and the nature of the bonding in the Ni/Gr junction can be obtained from calculating the charge transfer and the nonlocal binding energy density. We next discuss the first of them. The charge rearrangement is shown along the cutting plane marked by a green line along the unit cell diagonal in Fig. 7(a). From Fig. 7(b) it is clear that such a charge transfer differs significantly for C1 and C2 atoms, confirming again an inequivalent strength of the hybridization between Ni and Gr. C1, spatially closer to the interfacial Ni1, undergoes a stronger hybridization. Further insights into charge rearrangement are visible from isosurfaces for charge gain (red) and loss (blue), shown in Figs. 7(c) and 7(d), for side and top views.

From the appearance of the charge transfer in Fig. 7(b) one might conclude that there is a strong chemical interaction between Ni and graphene. However, as explained in Ref. [49], this system is better described as having a weak adsorption with strong interaction. Gr on Ni shows a subtle interplay of long-range vdW forces and short-range chemical interactions. To minimize the energy of this system, the vdW attraction brings Gr close to surface Ni atoms—at distances of 2.1 Å, typical for chemical bonds. At such proximity, an overlap of the orbitals between C and Ni atoms results in a charge rearrangement that, together with vdW interaction, brings the system to its energy minimum. While an overall weak adsorption of graphene on Ni can be quantified by a relatively small value of the binding energy, characteristic for the physisorption value, it is accompanied by a pronounced effect of chemical interaction visible both in the destruction of the Dirac cone (gap opening) at the K point and a significant charge transfer. A more detailed analysis shows that the vdW attraction is somewhat larger, while the charge rearrangement yields a repulsive contribution, resulting together in a total attractive binding of $\sim$70 meV/C atom at 2.1 Å. This is a slightly stronger binding than at another total energy minimum occurring at the Ni-C separation of around 3.1 Å, of a pure physisorption character and with a negligible interfacial charge rearrangement [49].

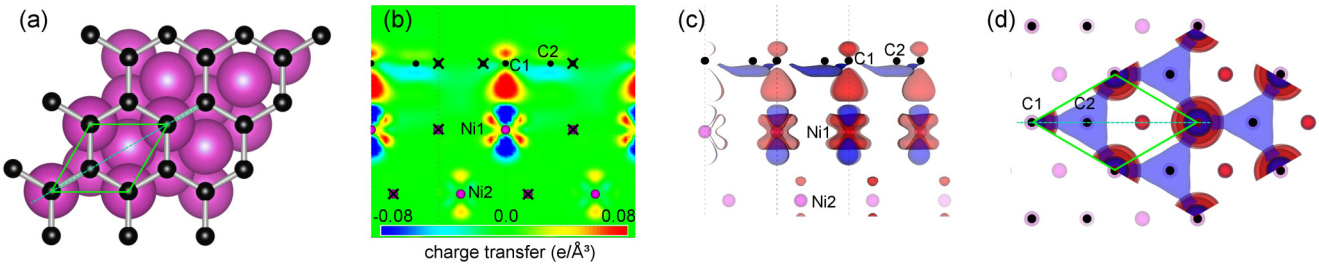

FIG. 7. (Color online) The charge rearrangement: Difference of charge densities of the system and its parts, (a) shown along the cutting plane through the marked green diagonal in the unit cell. (b) The color range from blue (charge loss) to red (charge gain) corresponds to charge transfer values from -0.08 to 0.08 $e/\text{Å}^3$, where e is the magnitude of the electron charge. Bold black and violet circles denote the C and Ni atoms in the cutting plane. Atoms outside that plane are marked with additional white crosses. Isosurfaces of values 0.03 (red, charge gain) and -0.03 (blue, charge loss) $e/\text{Å}^3$ are shown using side (c) and top (d) views. The charge density is repeated throughout several unit cells.

The Ni-C interaction is dominated by the hybridization between Gr π and Ni d_{z^2} orbitals. From the shape of the charge transfer isosurfaces and their cross section in Figs. 7(b) and 7(c), we conclude that the hybridization between top-site C1 and Ni1 atoms (p_z with d_{z^2} orbitals) results in a push of some Ni1 d_{z^2} orbitals above the Fermi level and thus a depletion of charge in those states and an increase of the charge density on the C1 p_z orbitals. The other carbon atom, C2 on a fcc site has a negligible interaction with the substrate, except through the charge rearrangement in the graphene layer itself, caused by the interaction of the on-top-site C1 atom with Ni.

We finally explore the nonlocal correlation binding energy, providing additional insights about the Ni-C interaction and the importance of the vdW bonding. This energy is expressed as the vdW-DF functional [50]

$$\begin{aligned} E_c^{NL} &= \frac{1}{2}\int\int d\vec{r}\,d\vec{r}\,' n(\vec{r})\phi(\vec{r},\vec{r}\,')n(\vec{r}\,') \\ &= \int d\vec{r}\left[\frac{1}{2}n(\vec{r})\int d\vec{r}\,'\phi(\vec{r},\vec{r}\,')n(\vec{r}\,')\right] \\ &= \int d\vec{r}\, e_c^{NL}(\vec{r}). \end{aligned} \tag{3}$$

Here n is the electron gas (number) density and ϕ is the kernel of a double-space integral [50]. The nonlocal correlation energy density per spatial point e_c^{NL} represents the difference between the system and its parts (Ni slab and Gr sheet) and enables us to visualize the distribution of the nonlocal correlation binding energy in Fig. 8. Since it is not possible to generate images of e_c^{NL} from VASP, we have used the JuNoLo code for that purpose [79].

A binding energy calculated from local or semilocal correlation functionals [using the local density approximation (LDA) or the generalized gradient approximation (GGA)], defined with a single-space integral, provides a simple interpretation: The correlation energy can be assigned to a particular spatial point. The nonlocal character of e_c^{NL} makes it more challenging to interpret its visualization: At each point it represents half of the energy of the interaction of that point with all the other points in space [80].

The vdW-DF has significant advantages over much simpler semiempirical approaches [81] to introduce the vdW interaction: (i) the vdW-DF seamlessly includes extreme bonding cases, from strong chemisorption (a large charge transfer, as in GGA or LDA) to strong physisorption (negligible charge transfer), and (ii) it reveals the origin of the vdW interaction from the electron gas (due to nonlocal correlations). In the semiempirical approaches atomic coordinates play a crucial role, one would expect that the vdW interaction is related to those positions.

However, Fig. 8 reveals a rather different picture. The regions of significant e_c^{NL} are distributed in strange shapes, even distant from the neighboring C atoms. Comparing Figs. 7(b) and 8(b) we see that a large e_c^{NL} corresponds well to the regions with the depleted charge after rearrangement. The origin of this behavior is subtle and related to the definition of the kernel ϕ in Eq. (3). The vdW-DF generalizes the analytical LDA solution for correlation (both local and nonlocal) in a homogeneous electron gas by using an expansion in inhomogeneous n. Unlike in GGA or LDA, nonlocal binding occurs even without charge rearrangement, for example, in regions left and right above Ni1 in Fig. 8(b). The charge surrounding is different between separated parts and the parts brought together to form the system.

If the charge rearrangement occurs, signaling chemical interaction, typically the dominant "lumps" of nonlocal correlation binding energy are found where the charge was depleted [82]. Again, this behavior is driven by the inhomogeneity introduced in the electron gas by charge transfer and by reducing n—it becomes more polarizable—which is at the heart of the vdW interaction. The vdW interaction is a product of polarizability and n. A large contribution is then a trade-off between a large n (yielding small polarizability) and a large polarizability (yielding small n). Intermediate densities bring the largest contributions and such densities seem to appear in regions of a depleted charge.

From the visualization of e_c^{NL}, we conclude that such an energy is relatively small per point, but is spread over a large area (volume). Thus, its total contribution to the binding energy is considerable, yet almost completely invisible for the local or semilocal functionals. By limiting the range of the interaction in Eq. (3), one could explicitly show [82] that the nonlocal binding energy stems from the interaction between the region around Gr and the region on the Ni surface, rather than from just one region.

Our detailed analysis of the computational geometry, including band structure, density of states, charge rearrangement, and the nonlocal correlation energy, shows that hybridization with Ni leads to the nontrivial changes in the electronic structure of graphene. Consequently, we expect that these changes will also influence various spin-dependent properties, such as spin injection and proximity effects, which

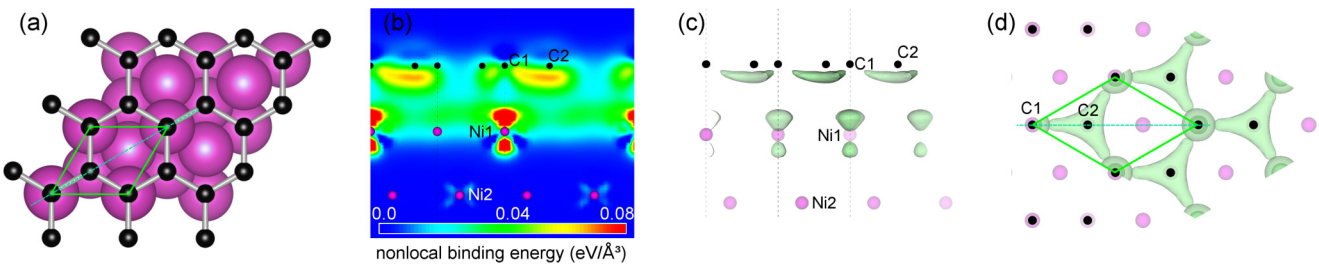

FIG. 8. (Color online) Nonlocal binding energy density e_c^{NL}, (a) shown along the cutting plane through the marked green diagonal in the unit cell. (b) e_c^{NL} spans the range from 0 (blue) to 80 (red) meV/Å^3. An isosurface of $e_c^{NL} = 60$ meV/Å^3 is shown using side (c) and top (d) views. The nonlocal binding energy density is repeated throughout several unit cells.

we will next try to estimate by introducing a computationally inexpensive model using equilibrium calculations and spin polarization maps.

IV. SPIN POLARIZATIONS: MODELING SPIN INJECTION AND PROXIMITY EFFECTS

Calculating spin polarizations accurately is an important prerequisite in the studies of various spintronic devices. It provides a method to parametrize spin injection (recall Sec. II) as well as various magnetoresistive and proximity effects. However, even for a uniform bulk material different experimental techniques can lead to different and inequivalent spin polarizations. A simple change of a nonmagnetic region, such as replacing a Al_2O_3 tunnel barrier by MgO [83–85], changes dramatically the effective spin polarization and tunneling magnetoresistance using conventional ferromagnetic regions. This highlights the need for accurate studies of interfacial properties in ferromagnetic junctions: Altering the interfacial configuration can significantly influence various spin-dependent properties.

While it is tempting, as is often done [21], to use the DOS spin polarization evaluated at the Fermi level ($E = 0$)

$$P_N = (N_\uparrow - N_\downarrow)/(N_\uparrow + N_\downarrow) \tag{4}$$

as a figure of merit for graphene spintronics, this quantity is generally not related to transport. Similar problems [85,86] pertain to the interpretation that P_N of a bulk ferromagnet should be used to parametrize the tunneling magnetoresistance (TMR) in Jullière's model [87,88]

$$\mathrm{TMR} = \frac{2P_{N1}P_{N2}}{1 - P_{N1}P_{N2}}, \tag{5}$$

where the ferromagnets F1 and F2 are separated by a tunnel barrier.

For Ni, which at the Fermi level has both heavy d and light s electrons, the DOS is dominated by the d electrons, while the transport is influenced by s electrons with a large Fermi velocity. As pointed out by Mazin [89], instead of using P_N, it is relevant to consider a different effective spin polarization,

$$P_{Nv^\alpha} = (\langle Nv^\alpha\rangle_\uparrow - \langle Nv^\alpha\rangle_\downarrow)/(\langle Nv^\alpha\rangle_\uparrow + \langle Nv^\alpha\rangle_\downarrow), \tag{6}$$

where the angular brackets denote performing the corresponding Fermi surface average, where $v_\uparrow$ and $v_\downarrow$ are the majority and minority Fermi velocities, respectively. $\alpha = 1$ or P_{Nv} applies to the ballistic transport, while $\alpha = 2$ or P_{Nv^2} yields the current polarization in the diffusive or tunneling regimes [89,90]. Specifically, when $\alpha = 1$ the expression for a spin-resolved current has the form $J_\lambda \propto \langle Nv_\lambda\rangle$, expected for a ballistic transport through a Sharvin contact [90], while choosing $\alpha = 2$ in performing the Fermi surface average leads to the spin-resolved current $J_\lambda \propto \langle Nv_\lambda^2\rangle$, consistent with the diffusive transport obtained from a Boltzmann transport equation [90,91]. Consequently, we can confirm the corresponding interpretations for the two spin polarizations $\alpha = 1,2$ in Eq. (6).

We first calculate the reference case of bulk Ni, shown in Fig. 9(a). Our vdW-DF results agree well with all the features obtained in Ref. [89]. Unless we are dealing with the half-metallic ferromagnet for which different definitions would lead to the same, complete polarization, even in a homogeneous bulk sample, P_N, P_{Nv}, and P_{Nv^2} can be very different and have a strong energy (bias) dependence. The trends for these spin polarizations also remain in the main panel of Fig. 9(b) showing results in the lowest energy Ni/Gr configuration, top-fcc depicted in Fig. 3(b).

Some care is needed to understand what is implied for the Fermi velocity in the F/Gr junction. Due to the two-dimensional character of graphene which at one of its ends is surrounded by vacuum, $v_z = 0$, normal to the interface. Unlike the depicted spin injection and transport *across* (normal) the interface in Fig. 1(a) we should think of spin injection and transport in the direction *parallel* to the F/Gr interface. Consequently, P_{Nv}, and P_{Nv^2} could be viewed as pertaining to the ballistic and diffusive, *parallel* to the interface. However, for a different geometry (to be discussed later, in Fig. 12) where the graphene region is surrounded by Ni slabs from both sides, there is a well-defined $v_z \neq 0$ and we expect the longitudinal transport *normal* to the interface.

We can now explore one of the contributions to the spatial nonuniformity of spin-dependent properties, influenced by the choice of substrate. The existence of a substrate-induced charge puddles (of size ~100 nm) will lead to a position-dependent Fermi level and spatially alter

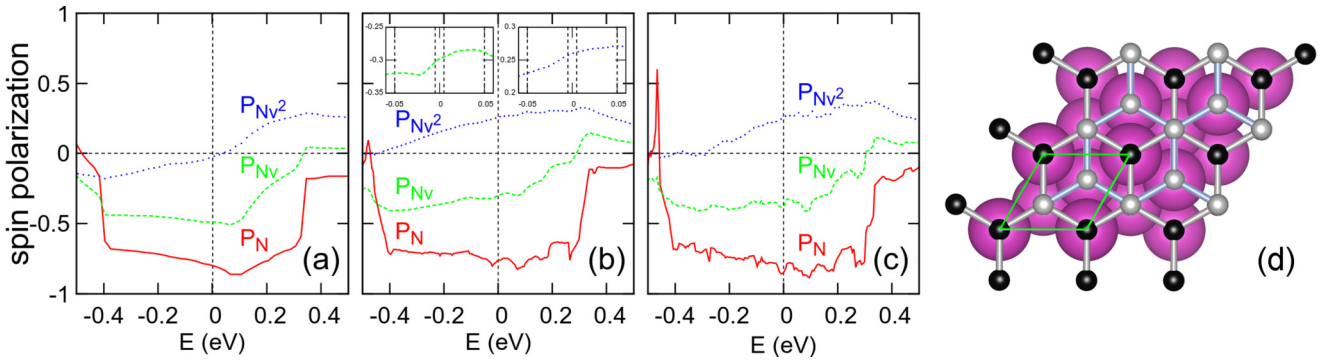

FIG. 9. (Color online) (a) Energy dependence of the spin polarizations P_N, P_{Nv}, and P_{Nv^2} in bulk Ni. (b) Results for top-fcc Ni/Gr. The inset marks (vertical lines) the relevant E variation of the Fermi level due to substrate-induced charge puddles [71] (10 meV for BN, 100 meV for SiO_2). (c) Ni/bilayer Gr, the first and second layers are top-fcc and hcp-fcc, respectively, corresponding to the AB stacking, as depicted in (d).

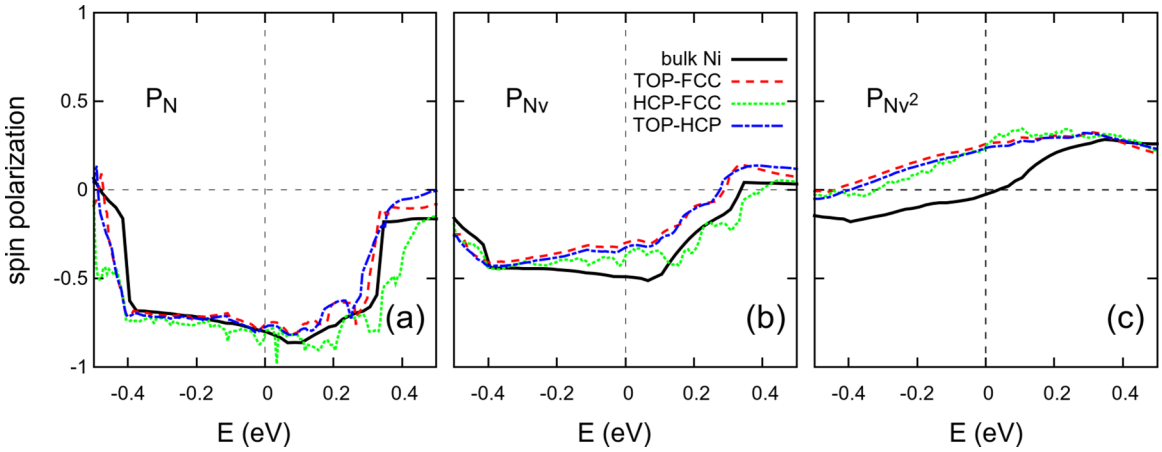

FIG. 10. (Color online) (a) Energy dependence of the spin polarizations (a) P_N, (b) P_{Nv}, and (c) P_{Nv^2} for the three lowest-energy Ni/Gr configurations: top-fcc, hcp-fcc, and top-hcp. Reference curves for bulk Ni are also shown.

the effective spin polarization. Using a relation between the effective spin polarization and spin injection, as discussed in Sec. II, we can also estimate the expected nonuniformity of spin injection across the Ni/Gr junction. The insets in Fig. 9(b) mark the energy intervals corresponding to the expected variation of the Fermi level with BN and SiO_2 substrates. BN [92,93] appears to be a good choice for achieving uniform spin injection and other spin-dependent properties [94]. Different substrates with a pronounced polar character strongly alter the magneto-optical conductivity of graphene [95].

Our choice of the vdW-DF is particularly suitable to examine multilayer graphene. We model adding another Gr layer (in the lowest configuration) by enlarging our computational cell to nine atoms: five Ni atoms and two C atoms per Gr layer. The interfacial configuration and calculated spin polarizations are given in Fig. 9(c). It is interesting to compare these results with a single Gr layer from Fig. 9(b). Even though adding two more nonmagnetic (C) atoms in the computational cell appears to be "magnetically diluting" our considered system, we see comparable spin polarizations and a slight increase in maximum P_{Nv^2}. Bilayer results show additional small features in all spin polarizations, consistent with the vdW bonding and the weaker hybridization of the Gr layer.

Recalling that a complete experimental F/Gr interface can include "mosaiclike" different epitaxial arrangements of graphene on Ni(111) (Fig. 3) of similar energies, we examine if they lead to significantly different spin polarizations which would imply a nonuniform spin injection. The results for the lowest energy configuration of a single layer Gr (top-fcc) are shown in Fig. 10, together with the two energetically higher configurations hcp-fcc (3.9 meV above) and top-hcp (15.9 meV above). The dominant contribution to P_N in Fig. 10(a) for all the studied configurations can be attributed to the bulk Ni behavior, shown as a reference solid curve. The departure from Ni behavior is more apparent in Fig. 10(c), as the contribution of the Fermi velocity grows for P_{Nv^2}.

For all P_N, P_{Nv}, and P_{Nv^2} the most similar behavior is between the lowest and highest energy configuration (top-fcc and top-hcp). How can we understand this seemingly peculiar trend? A closer analysis reveals that both top-fcc and top-hcp are examples of chemisorption with the bonding distance of ∼2.1 Å, while in hcp-fcc a chemisorption with a pronounced vdW character is responsible for a much larger distance of ∼3.1 Å. From P_N for hcp-fcc we also see more features than in the two chemisorption configurations where the stronger effect of hybridization between Ni and C atoms could be attributed to smoothing their individually different DOS behaviors. Only modest changes in P_{Nv^2} for different configurations are encouraging for the uniformity of spin injection in a diffusive regime.

We now return to the spin polarization of bilayer graphene [96], shown for the lowest-energy configuration in Fig. 9(c). Pristine bilayer Gr displays different intrinsic properties from pristine single layer Gr, such as an opening of the energy gap. Within our simplified computational geometry, studying a bilayer Gr may also reveal trends expected in the actual F/Gr junctions for spin injection in lateral devices [2,17,18] that can differ significantly from a vertical geometry with a single interface in Fig. 1(a). In such lateral devices the spin injection can be viewed as proceeding through two interfaces (junctions): (i) from F in contact with Gr, strongly modified by the proximity of the F region, and (ii) from strongly modified Gr to pristine Gr (for example, extending laterally beyond the region covered by a ferromagnet). Qualitatively, the influence of this second interface can be modeled as the "interface" between the first and the second Gr layer. Different bilayer configurations, shown in Fig. 11 and labeled by the first Gr layer (next to the Ni slab), could be viewed as altering the relative orientation of the second interface with respect to the pristine Gr.

The three bilayer configurations follow the same ordering in energy as a single Gr layer in Fig. 10. The lowest energy is for top-fcc, hcp-fcc is 15.8 meV above, and top-hcp is 21.6 meV above top-fcc. In all the cases, the distance of the second Gr layer is about 3.3 Å, approaching the layer separation in graphite. While for a single Gr layer there was a slight distinction between spin polarizations for chemisorption and physisorption (having additional small features, recall Fig. 10), there are no pronounced differences for bilayer Gr. All spin polarizations display similar trends. Connecting this behavior with the interpretation of the second interface relevant for spin injection in lateral F/Gr junctions, we expect a modest

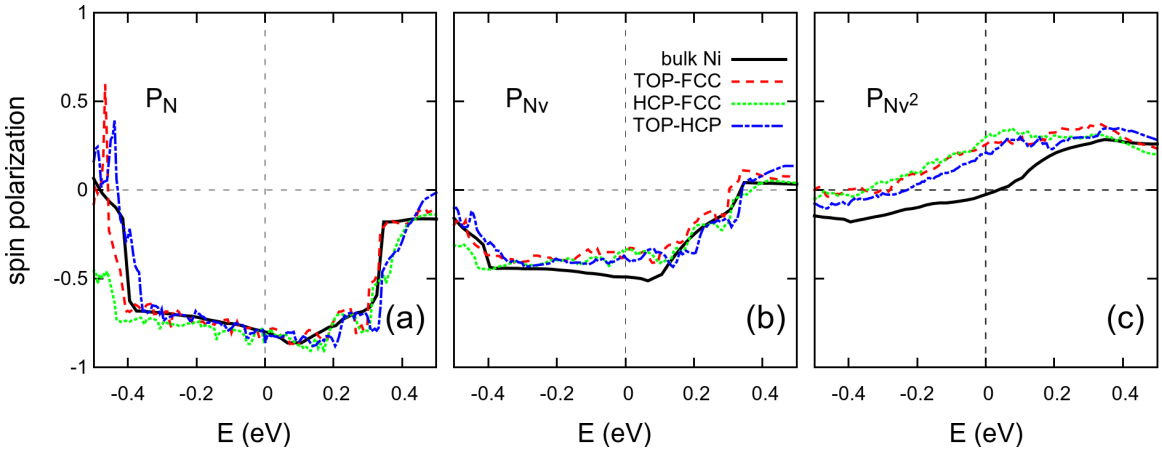

FIG. 11. (Color online) (a) Energy dependence of the spin polarizations (a) P_N, (b) P_{Nv}, and (c) P_{Nv^2} for the three lowest-energy Ni/bilayer Gr configurations: top-fcc, hcp-fcc, and top-hcp. The configurations are labeled by the first graphene layer (next to the Ni slab) and the same energy ordering is retained as in the single layer graphene from Fig. 10.

dependence of the spin injection on the orientation of this second interface.

In contrast to the previous geometries with vanishing Fermi velocity normal to the interface ($v_z = 0$), we can apply a similar framework to vertical Ni/Gr/Ni junctions (each Ni slab has five atoms) and also study properties relevant to vertical transport. We confirm in Fig. 12 a spin-filtering effect [7,10,97,98] with multilayer graphene. At the Fermi level, for a top-fcc interfacial configuration, P_{Nv_z} for five Gr layers (ABABA stacking) is almost one order of magnitude larger than for a single Gr layer. The magneto-optical Kerr effect can be a very sensitive probe to identify different stackings in multilayer Gr [99].

The results in Figs. 9–12 already provide some guidance about spin injection and its possible bias dependence arising from the energy-dependent DOS and Fermi velocities [100], missing in the simple model of spin injection. For an additional understanding of F/Gr spin injection in a diffusive regime, relevant to lateral spin transport and magnetologic gates, it could be possible to take advantage of state-of-the-art codes combining transport with first-principles electronic structure calculations [98,101]. This is a considerable challenge as such codes are computationally demanding and are typically tailored to ballistic transport. A further computational complexity will result from the effort to describe the diffusive regime. However, we show here that, even with a small computational cell and modest computational resources, we could provide considerably more detailed information then already available in Fig. 9.

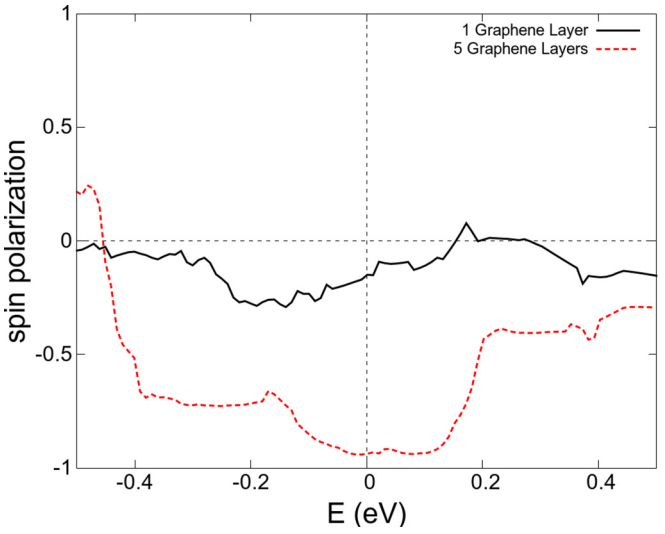

FIG. 12. (Color online) Spin-filtering effect in ballistic spin polarization across the Ni/Gr/Ni slab P_{Nv_z}.

From the simple picture of spin injection in Sec. II, one can infer that more representative information should be spatially resolved, rather than averaged over the whole junction, as in Fig. 9. On one hand, the information about the interfacial layer of Ni could be more important for spin injection, than bulk Ni properties, far away from the Ni/Gr junction. On the other hand, an average spin polarization over the whole junction is typically dominated by the bulk Ni properties with only a small contribution coming from the C atoms. As one is interested in lateral geometries, it is precisely that spin-dependent information induced on C atoms, away from the F region, that would be particularly relevant.

Such spatially resolved information is also crucial for the studies of proximity effects which are otherwise overshadowed by a large spin-dependent signal of the F region. Moreover, within our *equilibrium* calculations, exploring proximity effects is directly accessible. In novel material systems it may not be obvious what is the origin of the large changes (including a sign change) between different spin polarizations. To further explore that, as well as the dominant contribution to different spin polarizations, it is valuable to study their projection to different atomic orbital symmetries [102].

To better understand the spatially resolved information, we focus in Fig. 13 on the lowest-energy interfacial configuration (top-fcc) and show bulk Ni and atomically resolved magnetic moments. The interfacial Ni1 magnetic moment is reduced as compared to its bulk value, while the suppression is much stronger on the two C atoms (C1 and C2 have opposite signs). The middle panel of Fig. 13 shows the orbital projections of the DOS polarization. While C atoms are dominated by the

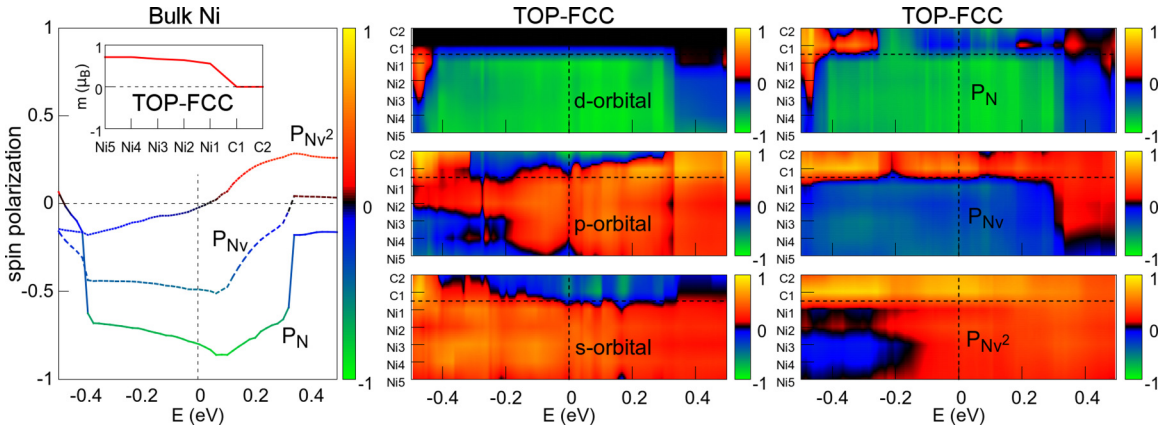

FIG. 13. (Color online) The anatomy of spin polarization. From left to right: Spin polarizations for a reference Ni bulk sample and the color scale used throughout. Inset: Magnetic moment resolved on each atom in the computational cell (C1, C2, Ni1, . . . ,Ni5) for top-fcc configurations. Orbital projections of the atomically resolved DOS spin polarization shown as a function of energy. In these and all the subsequent panels, the dashed horizontal line marks the Ni/Gr interface. Right panel: Spin polarization maps.

contributions of the s and p orbitals, the total DOS for Ni reflects the d-orbital contribution of the minority spin and thus leads to bulk $P_N < 0$.

If we use the Ni3 value (in the middle of the computational Ni slab) to represent a bulk DOS behavior, it reveals that a sharp bulk P_N increase (near $E \approx -0.4$ and 0.3 eV, left panel) coincides with the approximate width of the d band [89]. From the Ni3 DOS values we see that the subdominant s- and p-orbital contributions have an opposite sign to the dominant d-orbital contribution. However, once we consider the DOS convolution with the square of the Fermi velocity, the roles of subdominant and dominant contributions can be exchanged. For $E > 0$ the importance of the s contribution is responsible that $P_{Nv^2} > 0$ has an opposite sign to P_N.

Another way to examine spatially resolved spin polarizations is provided in the right panel of Fig. 13 where different orbital contributions are summed up and shown for P_N, P_{Nv}, and P_{Nv^2}, all corresponding to the lowest-energy interfacial configuration. A quick look confirms the expected bulk behavior of these polarizations (by looking at the behavior of the Ni3 values), as well as the similarity of the atomically resolved total P_N to just its d-orbital contribution.

To deduce possible trends in spin injection, we use the interfacial Ni1 value as its proxy. As a nonequilibrium process, the spin injection in the diffusive regime is better represented by P_{Nv^2} at Ni1 (and its energy/bias dependence), than by the Gr value at C1 and C2 which, at $E = 0$, corresponds to the intrinsically equilibrium proximity effects. Indeed, the spin diffusion length (recall Fig. 1), associated with spin injection/accumulation from a ferromagnet, exceeds microns in Gr, significantly longer than the Fermi wavelength [11,103,104] $\lambda_F \sim 50$ nm, characteristic for proximity effects.

Inferring spin injection through the Ni1 value of P_{Nv^2} suggest its modest efficiency. This is not surprising considering the simple resistor model of a F/Gr junction, in the absence of a large spin-dependent interfacial contribution. Similar difficulties, including magnetically inactive ferromagnetic/silicon interfaces were attributed to early failures to achieve spin injection in Si [105]. However, there are experiments showing a more complicated behavior and an efficient spin injection in the regime where the arguments of the resistance mismatch between the F and N regions would suggest negligible spin injection [56,106]. Furthermore, similar to spin filtering with additional Gr layers in Fig. 12, we expect that a more efficient spin injection using Ni would be readily available, without relying on conventional tunnel barriers. There are already experimental demonstrations of a robust spin injection inserting either a layer of amorphous C atoms or a layer of a fluorinated Gr in F/Gr junctions [19,20].

We can examine several factors that could contribute to the spatial dependence of the Ni1 value of P_{Nv^2} and thus to the nonuniformity of spin injection. Repeating the arguments about charge puddles from substrates that alter the position of the chemical potential, we expect that a weak energy dependence of P_{Nv^2} at Ni1 would be useful for realizing uniform spin injection. We note that both the magnitudes and the energy dependence of P_{Nv} and P_{Nv^2} of the bulk Ni3 values (right panel) match well with the actual bulk calculation in the left panel of Fig. 13.

In addition to the lowest-energy top-fcc, we also show in Fig. 14 the spin polarization maps for two higher energy interfacial configurations, top-hcp and hcp-fcc. A quick

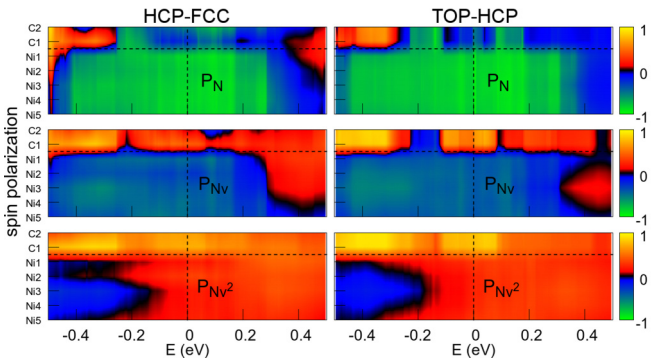

FIG. 14. (Color online) Spin polarization maps for interfacial configurations of higher energy, retaining the notation and color code from Fig. 12. Left panel: top-hcp, right panel: hcp-fcc interfacial configuration, from Figs. 3(c) and 3(d), respectively.

comparison with Fig. 13 reveals a very similar P_{Nv^2} for all considered configurations. Furthermore, at Ni1, proxy for spin injection, there is only a weak energy dependence. These findings are encouraging for a uniform spin injection across Ni/Gr junction in a diffusive regime. Even if we consider the substrate effects due to puddle formation, this would not alter significantly (especially for BN) the relevant spin polarization, supporting a uniform spin injection in the diffusive regime.

The spin polarization maps can also be used to examine magnetic proximity effects, arising from a nonvanishing overlap between the wave functions in the ferromagnetic and (initially) nonmagnetic regions, included in the first-principles calculations. While proximity effects alone can be viewed as central to several types of devices [12,44], we can also see their importance in including them for the studies of spin injection in F/Gr junctions.

The simple model of spin injection from Sec. II completely excludes magnetic proximity effects in the N region. For a thick N region in Fig. 1 this is a good approximation. Short-ranged proximity effects are localized in a very thin layer close to the F/N interface ($\sim\lambda_F$), while L_{sN} can be orders of magnitude longer: The nonequilibrium spin injection effects are predominantly responsible for any difference between the spin-up and spin-down properties, such as the DOS. In contrast, for the N region that is the 2D graphene layer, its thickness is smaller than the characteristic proximity length ($\lambda_F \sim 50$ nm in graphene). Even at zero bias, next to the ferromagnet, the whole N region acquires spin-dependent properties. The spin injection into Gr is then effectively a spin injection into a weak (proximity induced) magnet.

While in the top-fcc configuration (inset of Fig. 13, left panel) the magnetic moment induced on C1 and C2 is very small, the corresponding spin polarization is much larger. For the given energy range we see approximately that $P_N < P_{Nv} < P_{Nv^2}$, at both C1 and C2 positions. Considering that the magnetic proximity effect is even present in equilibrium and does not require transport, P_N is its useful signature. We can already infer some trends in the proximity effects from the charge transfer calculations in Fig. 7. Recognizing from Fig. 4(b) that the local environments are inequivalent for the C1 and C2 atomic sites we then expect a different charge transfer in these two sites. Indeed, while there is a strong charge transfer at C1, it is much smaller at C2.

Considering that a strong chemical bonding of the interfacial C and Ni atoms leads to a gap opening, we could expect an antiferromagnetic ordering in an insulator with a change of sign in P_N on C1 and C2. However, for the top-fcc configuration this is only realized in small pockets ($E \sim -0.3$ eV and $E \sim 0.4$ eV). The s-orbital contribution to the P_N has predominantly the same sign and there is a large positive P_{Nv^2} at both C1 and C2, for all shown energies. This behavior in which the sign of P_N on C1 and C2 is preserved could be explained by the change in the hybridization from sp^2, in pristine Gr, to sp^3, when Gr is bonded on Ni, consistent with the charge transfer in Fig. 7(b). A charge transfer in the region connecting C1 and Ni1 also indicates a change in the p_z orbital charge distribution, further supporting the assumption of an sp^3 bonding.

Another manifestation of the proximity effects can already be seen from the modification of the graphene band structure

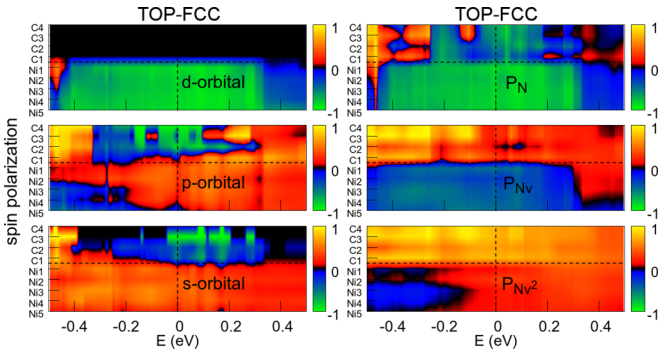

FIG. 15. (Color online) Spin polarization maps for top-fcc, the lowest interfacial configuration of a bilayer Gr. Left panel: Orbital projections of the atomically resolved DOS spin polarization, right panel: spin polarization maps.

in the Fig. 5. Top-fcc configuration in Ni/Gr junctions with a Ni1-C1 bonding distance of ≈2.1 Å leads to the destruction of the Dirac cone at the K point for freestanding graphene in Fig. 4. Using the parametrization from the proximity effects studied in a ferromagnetic insulator (EuO)/Gr junction [14], the modified Dirac dispersion relation at the K point contains the spin-dependent Fermi velocity $v_\uparrow/v_\downarrow \approx 11$ and the spin-dependent gap (mass) $\Delta_\uparrow \approx 380$ meV and $\Delta_\downarrow \approx 360$ meV, for majority and minority spin, respectively.

Spin polarization maps can also be used to explore junctions with bilayer Gr. This is informative both to further understand the proximity effect on C atoms, as well as to develop some insights about lateral spin injection that could be considered as being influenced by two interfaces (recall the discussion of Fig. 11). The results for the lowest-energy configuration in Fig. 15 clearly show that adding an extra layer of Gr (atoms C3 and C4), to the interfacial configuration top-fcc, leaves virtually unchanged not only the spin polarization on Ni atoms, but also on C1 and C2, from Fig. 13. This behavior also applies to the higher-energy configurations in Fig. 16.

Looking at the spin polarization maps for bilayer Gr one can predominantly see a continuous extension of features obtained with a single layer into the second layer. This behavior is a consequence of the strongly interacting p_z orbitals of the C atoms with the d_z^2 orbitals of the underlying Ni atoms.

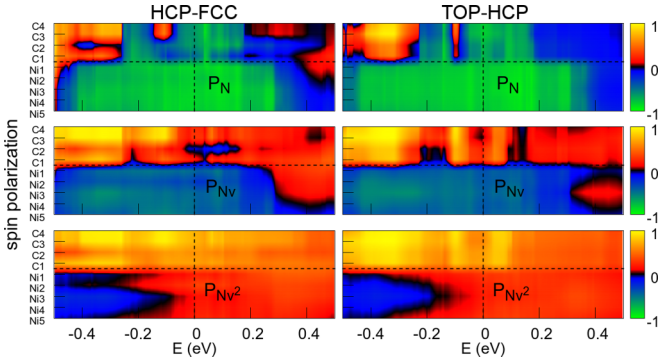

FIG. 16. (Color online) Spin polarization maps for interfacial configurations of higher energy and bilayer Gr. Left panel: top-hcp, right panel: hcp-fcc interfacial configuration.

The same orbitals in the second Gr layer are sensitive to those changes due to symmetry reasons, propagating them in Gr layers further away from the interface with Ni, even though the interaction between the first and second Gr layer is almost exclusively of vdW nature. For a given type of spin polarization (P_N, P_{Nv}, or P_{Nv^2}) we see only modest changes among different configurations of the second Gr layer. If we interpret that as the behavior representing the second interface, we expect only a small influence of the orientation of that interface on spin transport. These findings from spin polarization maps further corroborate our conclusions of the spatially averaged information presented in Fig. 11.

The information about the energy dependence contained in the spin polarization maps could be used to estimate the possibility to alter the magnetic proximity effects using a gate bias from an electrode placed close to the F region. Such tunable magnetic proximity effects are considered as a promising path to implement various spintronic devices [11–13].

V. CONCLUSIONS

We have established a computationally inexpensive model to explore spin injection and proximity effects from first principles. We illustrate our approach on the example of a Ni(111)/graphene junction and compare our findings with the standard model of spin injection, successfully employed for macroscopic metallic junctions. While that conventional picture of spin injection is bias independent and corresponds to an equivalent resistor scheme, our findings reveal that significant deviations from that description could be possible in Ni/graphene junctions. We explore several sources of the bias dependence and estimate different contributions to the nonuniformity of spin injection along the interface, important for spintronic devices, but absent in the conventional picture.

The two-dimensional nature of graphene requires reconsidering usually ignored proximity effects in the description of spin injection. The length scale of these proximity effects exceeds the thickness of graphene. The spin injection from a ferromagnet therefore takes place in a weak (proximity induced) magnet, rather than in a nonmagnetic material without any spin-dependent properties. For spin injection in lateral devices it is helpful to consider the influence of two interfaces: between Ni and strongly modified graphene and between strongly modified and (nearly) pristine graphene. From the studies of bilayer graphene, we conclude that main effects on spin injection come from the first interface.

To study spin injection and proximity effects we calculate different spin polarizations, that of the density of states, as well as ones including convolutions with the linear and quadratic contribution of Fermi velocities, for ballistic and diffusive regime, respectively. In addition to the results averaged over the whole junction, we also calculate atomically resolved spin polarization maps, providing the anatomy of spin polarization for a given interfacial configuration. This is particularly useful to study the effects on graphene layers, which otherwise could be very small if only the spin polarization of a whole junction is given.

Our approach complements other studies of spin injection and includes also a diffusive regime, usually not considered in the first-principles studies of spin transport. For simple models, described in Sec. II, our approach could provide various spin polarizations and their bias dependence, as required input parameters. This is applicable to models of lateral spin injection [67] where our findings could identify the missing bias dependence [107]. The efficiency of our first-principles description of spin injection provides a valuable guidance, before investing a large amount of computer time in more sophisticated quantum transport calculations [98,101] that give an accurate account of finite-bias effects in the ballistic regime, as well as a starting point for detailed studies in more complex systems [108,109].

We expect that various generalizations of our model could be directly implemented. The presence of surface roughness, disorder, and interfacial defects [45,110] modify spin polarizations and thus influence spin injection and proximity effects. Intercalation of other atoms in the interfacial region could significantly alter the spin-dependent properties of Gr junctions, hydrogenated graphene [65,111,112] provides one such example. In the context of spin injection efficiency, similar trends can already be inferred from Fe/GaAs junctions with intermixed interfacial configurations [45].

While we have focused on graphene-based junctions, our approach could be applied to a wide range of material systems to study their potential for spin-based devices. The use of van der Waals interactions in first-principles studies offers a natural framework both for the inclusion of important effects in multilayer graphene and the consideration of high-quality van der Waals 2D heterostructures [113], which are not limited to the lattice-matching constraints in conventional epitaxial growth.

ACKNOWLEDGMENTS

We thank K. D. Belashchenko, H. Dery, J. Fabian, I. I. Mazin, B. K. Nikolić, B. Scharf, L. J. Sham, and S. O. Valenzuela for valuable discussions. We thank the referees for their valuable suggestions. This work was supported by the US ONR N000141310754, NSF DMR-1124601, NSF ECCS-1102092, FAPESP (#2011/19333-4), CNPq (#246549/2012-2), and the Center for Computational Research, University at Buffalo.

[1] W. Hill, A. K. Geim, K. S. Novoselov, F. Schedin, and P. Blake, IEEE Trans. Magn. **42**, 2694 (2006).

[2] N. Tombros, C. Józsa, M. Popinciuc, H. T. Jonkman, and B. J. van Wees, Nature (London) **448**, 571 (2007).

[3] S. Cho, Y.-F. Chen, and M. S. Fuhrer, Appl. Phys. Lett. **91**, 123105 (2007).

[4] M. Nishioka and A. M. Goldman, Appl. Phys. Lett. **90**, 252505 (2007).

[5] M. Ohishi, M. Shiraishi, R. Nouchi, T. Nozaki, T. Shinjo, and Y. Suzuki, Jpn. J. Appl. Phys. Part 2 **46**, L605 (2007).

[6] W. H. Wang, K. Pi, Y. Li, Y. F. Chiang, P. Wei, J. Shi, and R. K. Kawakami, Phys. Rev. B **77**, 020402(R) (2008).

[7] V. M. Karpan, G. Giovannetti, P. A. Khomyakov, M. Talanana, A. A. Starikov, M. Zwierzycki, J. van den Brink, G. Brocks, and P. J. Kelly, Phys. Rev. Lett. **99**, 176602 (2007).

[8] O. M. J. van't Erve, A. L. Friedman, E. Cobas, C. H. Li, J. T. Robinson, and B. T. Jonker, Nat. Nanotech. **7**, 737 (2012).

[9] H. Dery, Nat. Nanotech. **7**, 692 (2012).

[10] E. Cobas, A. L. Friedman, O. M. J. van't Erve, J. T. Robinson, and B. T. Jonker, Nano Lett. **12**, 3000 (2012).

[11] H. Haugen, D. Huertas-Hernando, and A. Brataas, Phys. Rev. B **77**, 115406 (2008).

[12] Y. G. Semenov, K. W. Kim, and J. M. Zavada, Appl. Phys. Lett. **91**, 153105 (2007).

[13] Y. G. Semenov, J. M. Zavada, and K. W. Kim, Phys. Rev. Lett. **101**, 147206 (2008).

[14] H. X. Yang, A. Hallal, D. Terrade, X. Waintal, S. Roche, and M. Chshiev, Phys. Rev. Lett. **110**, 046603 (2013).

[15] A. G. Swartz, P. M. Odenthal, Y. Hao, R. S. Ruoff, and R. K. Kawakami, ACS Nano **6**, 10063 (2012).

[16] P. Michetti and P. Recher, Phys. Rev. B **84**, 125438 (2011).

[17] W. Han, K. Pi, K. M. McCreary, Y. Li, J. J. I. Wong, A. G. Swartz, and R. K. Kawakami, Phys. Rev. Lett. **105**, 167202 (2010); W. Han, K. M. McCreary, K. Pi, W. H. Wang, Y. Li, H. Wen, J. R. Chen, and R. K. Kawakami, J. Magn. Magn. Mater. **324**, 369 (2012).

[18] P. Seneor, B. Dlubak, M.-B. Martin, A. Anane, H. Jaffres, and A. Fert, MRS Bull. **37**, 1245 (2012), and the references therein.

[19] I. Neumann, M. V. Costache, G. Bridoux, J. F. Sierra, and S. O. Valenzuela, Appl. Phys. Lett. **103**, 112401 (2013).

[20] A. L. Friedman, O. M. J. van't Erve, C. H. Li, J. T. Robinson, and B. T. Jonker, Nat. Commun. **5**, 3161 (2014).

[21] I. Žutić, J. Fabian, and S. Das Sarma, Rev. Mod. Phys. **76**, 323 (2004).

[22] J. Fabian, A. Matos-Abiague, C. Ertler, P. Stano, and I. Žutić, Acta Phys. Slov. **57**, 565 (2007).

[23] H. Dery, H. Wu, B. Ciftcioglu, M. Huang, Y. Song, R. Kawakami, J. Shi, I. Krivorotov, I. Žutić, Lu J. Sham, IEEE Trans. Electron. Dev. **59**, 259 (2012); H. Dery, H. Wu, B. Ciftcioglu, M. Huang, Y. Song, R. K. Kawakami, J. Shi, I. N. Krivorotov, D. A. Telesca, I. Žutić, and L. J. Sham, Proc. SPIE **8100**, 81000W (2011).

[24] H. Dery, P. Dalal, L. Cywinski, and L. J. Sham, Nature (London) **447**, 573 (2007).

[25] M. Johnson and R. H. Silsbee, Phys. Rev. Lett. **55**, 1790 (1985).

[26] C. Józsa and B. J. van Wees, in *Handbook of Spin Transport and Magnetism*, edited by E. Y. Tsymbal and I. Žutić (CRC Press, New York, 2011).

[27] Y. Otani and T. Kimura, in *Handbook of Spin Transport and Magnetism*, edited by E. Y. Tsymbal and I. Žutić (CRC Press, New York, 2011).

[28] J. Rudolph, D. Hägele, H. M. Gibbs, G. Khitrova, and M. Oestreich, Appl. Phys. Lett. **82**, 4516 (2003); J. Rudolph, S. Döhrmann, D. Hägele, M. Oestreich, and W. Stolz, *ibid.* **87**, 241117 (2005).

[29] M. Holub, J. Shin, D. Saha, and P. Bhattacharya, Phys. Rev. Lett. **98**, 146603 (2007).

[30] N. C. Gerhardt, M. Y. Li, H. Jähme, H. Höpfner, T. Ackemann, and M. R. Hofmann, Appl. Phys. Lett. **99**, 151107 (2011).

[31] S. Iba, S. Koh, K. Ikeda, and H. Kawaguchi, Appl. Phys. Lett. **98**, 081113 (2011).

[32] C. Gø thgen, R. Oszwałdowski, A. Petrou, and I. Žutić, Appl. Phys. Lett. **93**, 042513 (2008).

[33] I. Vurgaftman, M. Holub, B. T. Jonker, and J. R. Mayer, Appl. Phys. Lett. **93**, 031102 (2008).

[34] J. Lee, W. Falls, R. Oszwałdowski, and I. Žutić, Appl. Phys. Lett. **97**, 041116 (2010).

[35] D. Saha, D. Basu, and P. Bhattacharya, Phys. Rev. B **82**, 205309 (2010).

[36] R. Al-Seyab, D. Alexandropoulos, I. D. Henning, and M. H. Adams, IEEE Photon. J. **3**, 799 (2011).

[37] J. Lee, R. Oszwałdowski, C. Gøthgen, and I. Žutić, Phys. Rev. B **85**, 045314 (2012).

[38] D. Banerjee, R. Adari, M. Murthy, P. Suggisetti, S. Ganguly, and D. Saha, J. Appl. Phys. **109**, 07C317 (2011).

[39] G. Boéris, J. Lee, K. Výborný, and I. Žutić, Appl. Phys. Lett. **100**, 121111 (2012).

[40] H. Höpfner, M. Lindemann, N. C. Gerhardt, and M. R. Hofmann, Appl. Phys. Lett. **104**, 022409 (2014).

[41] H. Dery, Y. Song, P. Li, and I. Žutić, Appl. Phys. Lett. **99**, 082502 (2011).

[42] D. A. B. Miller, Proc. IEEE **97**, 1166 (2009).

[43] The spin-orbit gap that is only $\sim$24 μe. M. Gmitra, S. Konschuh, C. Ertler, C. Ambrosch-Draxl, and J. Fabian, Phys. Rev. B **80**, 235431 (2009).

[44] C. Ciuti, J. P. McGuire, and L. J. Sham, Appl. Phys. Lett. **81**, 4781 (2002).

[45] T. J. Zega, A. T. Hanbicki, S. C. Erwin, I. Žutić, G. Kioseoglou, C. H. Li, B. T. Jonker, and R. M. Stroud, Phys. Rev. Lett. **96**, 196101 (2006).

[46] P. Mavropoulos, N. Papanikolaou, and P. H. Dederichs, Phys. Rev. Lett. **85**, 1088 (2000).

[47] J. P. Perdew, J. A. Chevary, S. H. Vosko, K. A. Jackson, M. R. Pederson, D. J. Singh, and C. Fiolhais, Phys. Rev. B **46**, 6671 (1992).

[48] P. Lazić, N. Atodiresei, V. Caciuc, R. Brako, B. Gumhalter, and S. Blügel, J. Phys.: Condens. Matter **24**, 424215 (2012).

[49] F. Mittendorfer, A. Garhofer, J. Redinger, J. Klimeš, J. Harl, and G. Kresse, Phys. Rev. B **84**, 201401(R) (2011).

[50] M. Dion, H. Rydberg, E. Schröder, D. C. Langreth, and B. I. Lundqvist, Phys. Rev. Lett. **92**, 246401 (2004).

[51] D. Eom, D. Prezzi, K. T. Rim, H. Zhou, M. Lefenfeld, S. Xiao, C. Nuckolls, M. S. Hybertsen, T. F. Heinz, and G. W. Flynn, Nano Lett. **9**, 2844 (2009).

[52] G. M. Sipahi, I. Žutić, N. Atodiresei, R. K. Kawakami, and P. Lazić, J. Phys.: Condens. Matter **26**, 104204 (2014).

[53] E. I. Rashba, Phys. Rev. B **62**, R16267 (2000).

[54] E. I. Rashba, Eur. Phys. J. B **29**, 513 (2002).

[55] S. Garzon, I. Žutić, and R. A. Webb, Phys. Rev. Lett. **94**, 176601 (2005).

[56] K. D. Belashchenko, J. K. Glasbrenner, and A. L. Wysocki, Phys. Rev. B **86**, 224402 (2012).

[57] Even in all-metallic junctions the differences can be great between the F region with $L_{sF} \sim 10$ nm for Co, Py, or Ni, and the N region with $L_{sF} \sim$ 100–1000 nm for Al or Cu at 300 K.

[58] As discussed in Ref. [21], this equation can be mapped to Eq. (A11) from M. Johnson and R. H. Silsbee, Phys. Rev. B **35**, 4959 (1987). An equivalent form was also obtained in S. Hershfield and H. L. Zhao, *ibid.* **56**, 3296 (1997).

[59] B. T. Jonker, S. C. Erwin, A. Petrou, and A. G. Petukhov, MRS Bull. **28**, 740 (2003).

[60] While it is often suggested that this obstacle can be removed using half-metallic ferromagnets, a careful analysis of Ref. [56] reveals subtleties in this argument.

[61] A similar result was recognized using the arguments of irreversible thermodynamics to study spin injection. M. Johnson and R. H. Silsbee, Phys. Rev. B **37**, 5312 (1988).

[62] I. Žutić, J. Fabian, and S. Das Sarma, Phys. Rev. Lett. **88**, 066603 (2002).

[63] I. Žutić, J. Fabian, and S. Das Sarma, Phys. Rev. B **64**, 121201 (2001).

[64] C. Jozsa, M. Popinciuc, N. Tombros, H. T. Jonkman, and B. J. van Wees, Phys. Rev. B **79**, 081402(R) (2009).

[65] M. Wojtaszek, I. J. Vera-Marun, T. Maassen, and B. J. van Wees, Phys. Rev. B **87**, 081402 (2013).

[66] F. Volmer, M. Drögeler, E. Maynicke, N. von den Driesch, M. L. Boschen, G. Güntherodt, and B. Beschoten, Phys. Rev. B **88**, 161405(R) (2013).

[67] S. Takahashi and S. Maekawa, Phys. Rev. B **67**, 052409 (2003).

[68] Gr itself can be effectively used as a tunnel barrier and enhance spin injection [8].

[69] Y. Murata, V. Petrova, B. B. Kappes, A. Ebnonnasir, I. Petrov, Y.-H. Xie, C. V. Ciobanu, and S. Kodambaka, ACS Nano **4**, 6509 (2010).

[70] Y. S. Dedkov and M. Fonin, New J. Phys. **12**, 125004 (2010).

[71] S. Das Sarma, S. Adam, E. H. Hwang, and E. Rossi, Rev. Mod. Phys. **83**, 407 (2011).

[72] W. Kohn and L. J. Sham, Phys. Rev. **140**, A1133 (1965).

[73] P. E. Blochl, Phys. Rev. B **50**, 17953 (1994).

[74] G. Kresse and J. Hafner, Phys. Rev. B **47**, 558 (1993).

[75] G. Kresse and J. Furthmüller, Phys. Rev. B **54**, 11169 (1996).

[76] H. J. Monkhorst and J. D. Pack, Phys. Rev. B **13**, 5188 (1976).

[77] Without the vdW. method, Ni/Gr junction was studied even before the graphene research was well established. G. Bertoni, L. Calmels, A. Altibelli, and V. Serin, Phys. Rev. B **71**, 075402 (2005). A recent work is T. Abtew, B.-C. Shih, S. Banerjee, and P. Zhang, Nanoscale **5**, 1902 (2013).

[78] In earlier vdW-DF implementations, the C1-Ni1 binding distance was ∼50% larger than in experiments, M. Vanin, J. J. Mortensen, A. K. Kelkkanen, J. M. Garcia-Lastra, K. S. Thygesen, and K. W. Jacobsen, Phys. Rev. B **81**, 081408(R) (2010).

[79] P. Lazić, N. Atodiresei, M. Alaei, V. Caciuc, S. Blügel, and R. Brako, Comput. Phys. Commun. **181**, 371 (2010).

[80] The vdW-DF functional contains two contributions to the correlation energy: (i) LDA of the homogeneous electron gas—both local and nonlocal, because the LDA is the analytical solution for a homogeneous electron gas. (ii) A nonlocal contribution to the inhomogeneous deviation in n, given in Eq. (3). Consequently, very close points in space will not have a large mutual nonlocal correlation energy contribution. Typically such points in space are of similar n, covered by the LDA part. The most prominent contributions in e_c^{NL} will appear in parts of the system which are brought closer together so that they interact via the vdW interaction.

[81] S. Grimme, J. Comput. Chem. **25**, 1463 (2004); **27**, 1787 (2006).

[82] Such a depleted charge tends to have two spatially close lumps. A more elaborate analysis reveals that a significant contribution to the interaction is intralump, rather than interlump. P. Lazić, M. Alaei, N. Atodiresei, V. Caciuc, R. Brako, and S. Blügel, Phys. Rev. B **81**, 045401 (2010); K. Berland and P. Hyldgaard, *ibid.* **87**, 205421 (2013).

[83] W. H. Butler, X.-G. Zhang, T. C. Schulthess, and J. M. MacLaren, Phys. Rev. B **63**, 054416 (2001).

[84] S. S. P. Parkin, C. Kaiser, A. Panchula, P. M. Rice, B. Hughes, M. Samant, and S.-H. Yang, Nat. Mater. **3**, 862 (2004); S. Yuasa, T. Nagahama, A. Fukushira, Y. Suzuki, and K. Ando, *ibid.* **3**, 868 (2004).

[85] K. D. Belashchenko and E. Y. Tsymbal, in *Handbook of Spin Transport and Magnetism*, edited by E. Y. Tsymbal and I. Žutić (CRC Press, New York, 2011); T. S. Santos and J. Moodera, *ibid.*

[86] X.-G. Zhang and W. H. Butler, J. Phys.: Condens. Matter. **15**, R1603 (2003).

[87] M. Julliére, Phys. Lett. A **54**, 225 (1975).

[88] S. Maekawa and U. Gäfvert, IEEE Trans. Magn. **18**, 707 (1982).

[89] I. I. Mazin, Phys. Rev. Lett. **83**, 1427 (1999).

[90] B. E. Nadgorny, in *Handbook of Spin Transport and Magnetism*, edited by E. Y. Tsymbal and I. Žutić (CRC Press, New York, 2011).

[91] We assume that the relaxation time is spin independent [89,90].

[92] C. R. Dean, A. F. Young, I. Meric, C. Lee, L. Wang, S. Sorgenfrei, K. Watanabe, T. Taniguchi, P. Kim, K. L. Shepard, and J. Hone, Nat. Nanotechnol. **5**, 722 (2010).

[93] A. S. Mayorov, R. V. Gorbachev, S. V. Morozov, L. Britnell, R. Jalil, L. A. Ponomarenko, P. Blake, K. S. Novoselov, K. Watanabe, T. Taniguchi, and A. K. Geim, Nano Lett. **11**, 2396 (2011).

[94] T. Yamaguchi, Y. Inoue, S. Masubuchi, S. Morikawa, M. Onuki, K. Watanabe, T. Taniguchi, R. Moriya, and T. Machida, Appl. Phys. Exp. **6**, 073001 (2013).

[95] B. Scharf, V. Perebeinos, J. Fabian, and I. Žutić, Phys. Rev. B **88**, 125429 (2013).

[96] Robust spin injection was also demonstrated in bilayer graphene-based lateral spin valves. I. Neumann, J. Van de Vondel, G. Bridoux, M. V. Costache, F. Alzina, C. M. Sotomayor Torres, and S. O. Valenzuela, Small **9**, 156 (2013).

[97] T. Banerjee, W. G. van der Wiel, and R. Jansen, Phys. Rev. B **81**, 214409 (2010).

[98] K. K. Saha, A. Blom, K. S. Thygesen, and B. K. Nikolić, Phys. Rev. B **85**, 184426 (2012).

[99] C. T. Ellis, A. V. Stier, M.-H. Kim, J. G. Tischler, E. R. Glaser, R. L. Myers-Ward, J. L. Tedesco, C. R. Eddy Jr, D. K. Gaskill, and J. Cerne, Sci. Rep. **3**, 3143 (2013).

[100] If a tunneling barrier is added, even a free-electron DOS leads to a bias-dependent spin injection. S. O. Valenzuela, D. J. Monsma, C. M. Marcus, V. Narayanamurti, and M. Tinkham, Phys. Rev. Lett. **94**, 196601 (2005).

[101] J. Maassen, W. Ji, and H. Guo, Nano Lett. **11**, 151 (2011); K. Dolui, A. Narayan, I. Rungger, and S. Sanvito, Phys. Rev. B **90**, 041401(R) (2014); Y.-P. Wang, J. N. Fry, and H.-P. Cheng, *ibid.* **88**, 125428 (2013).

[102] While the band structure would also provide a similar information, such representation tend to be overcrowded and lack the transparency afforded by the projection to different orbital symmetries.

[103] Y. Zheng, Y.-W. Tan, H. L. Stormer, and P. Kim, Nature (London) **438**, 201 (2005).

[104] M. I. Katsnelson, K. S. Novoselov, and A. K. Geim, Nat. Phys. **2**, 620 (2006).

[105] I. Žutić, J. Fabian, and S. C. Erwin, Phys. Rev. Lett. **97**, 026602 (2006).

[106] G. Bridoux, M. V. Costache, J. Van de Vondel, I. Neumann, and S. O. Valenzuela, Appl. Phys. Lett. **99**, 102107 (2011); T. Kimura, N. Hashimoto, S. Yamada, M. Miyao, and K. Hamaya, NPG Asia Mater. **4**, e9 (2012); K. Hamaya, N. Hashimoto, S. Oki, S. Yamada, M. Miyao, and T. Kimura, Phys. Rev. B **85**, 100404(R) (2012); M. Ramsteiner, O. Brandt, T. Flissikowski, H. T. Grahn, M. Hashimoto, J. Herfort, and H. Kostial, *ibid.* **78**, 121303(R) (2008).

[107] Strong nonlinearities in lateral spin injection using Co/Gr junctions are observed both as a function of an applied bias and gate voltage. T. Zhu and H. Wen (private communication).

[108] K. V. Raman, A. M. Kamerbeek, A. Mukherjee, N. Atodiresei, T. K. Sen, P. Lazić, V. Caciuc, R. Miche, D. Stalke, S. K. Mandal, S. Blügel, M. Munzenberg, and J. S. Moodera, Nature (London) **493**, 509 (2013).

[109] M. H. D. Guimarães, P. J. Zomer, J. Ingla-Aynés, J. C. Brant, N. Tombros, and B. J. van Wees, arXiv:1406.4656.

[110] R. M. Stroud, A. T. Hanbicki, Y. D. Park, G. Kioseoglou, A. G. Petukhov, B. T. Jonker, G. Itskos, and A. Petrou, Phys. Rev. Lett. **89**, 166602 (2002).

[111] K. M. McCreary, A. G. Swartz, W. Han, J. Fabian, and R. K. Kawakami, Phys. Rev. Lett. **109**, 186604 (2012).

[112] D. Soriano, F. Munõz-Rojas, J. Fernández-Rossier, and J. J. Palacios, Phys. Rev. B **81**, 165409 (2010); T. Kato, T. Nakamura, J. Kamijyo, T. Kobayashi, Y. Yagi, and J. Haruyama, Appl. Phys. Lett. **104**, 252410 (2014).

[113] A. K. Geim and I. V. Grigorieva, Nature (London) **499**, 419 (2013).